Flow over a single dimple recessed in a flat plate

Jianxun Zhu (朱建勋),[1, a)] Cai Tian (田偲),[1] and Lars Erik Holmedal[1]

1. Department of Marine Technology, Norwegian University of Science and Technology, 7052, Trondheim, Norway

(Dated: 26 December 2023)

Direct numerical simulations have been conducted to investigate a zero-pressure-gradient boundary layer flow over a single shallow dimple. Here the dimple depth to dimple diameter ratio (d/D) as well as the Reynolds number (based on D and free-stream velocity) are fixed at 0.05 and 20000, respectively. The effect of inlet boundary layer thickness δ on a given dimple is investigated by considering $\delta/D \in [0.023, 0.1]$. The flow within the dimple exhibits either a horseshoe vortex (a continuous core line through the two spirals within the dimple) or a tornado-like vortex pair (discontinuous core line). For the given parameter range, four different flow patterns have been identified within the single dimple; *i*) a steady symmetric horseshoe vortex pattern for $\delta/D \in [0.053, 0.1]$; *ii*) a steady asymmetric horseshoe vortex pattern for $\delta/D = 0.04$; *iii*) a quasi-periodic asymmetric horseshoe vortex pattern for $\delta/D = 0.033$; *iv*) a mixed horseshoe and tornado-like vortex pattern for $\delta/D = 0.023$. The growth of the streamwise vorticity, mainly caused by the tilting of the vertical vorticity, plays a key role in the transition between the different flow patterns. Dimple-induced velocity streaks above the single dimple have been investigated in detail for the first time, showing four different streaks; *i*) a High-speed streak above the dimple; *ii*) two Side-low-speed streaks located outside the dimple span; *iii*) two Side-high-speed streaks and *iv*) a Mid-low-speed streak in between them. These are mainly caused by a flow acceleration effect and a flow diffuser effect over the dimple, as well as a 'lift-up' mechanism within the downstream part of the dimple, tilting the boundary layer upwards.

[a)] Corresponding author: jianxun.zhu@ntnu.no

I. INTRODUCTION

Dimple geometry as a passive flow control strategy has been widely investigated both numerically and experimentally due to its practical applications such as, e.g., enhancing the heat-transfer rate[1,2], improving the aerodynamic performance of a wind turbine blade[3–5] and airfoils[6] as a vortex generator, trailing-edge noise reduction on the airfoil[7], as well as its potential application in drag reduction[8–10]. Despite these applications and the previous research associated with them, the basic physical mechanisms of flow over dimples are yet to be fully understood. The purpose of the present paper is to fill in some of this knowledge gap by investigating the detailed laminar flow over one single dimple using direct numerical simulations, which allow us to provide a building stone for understanding the flow over multiple dimples.

Previous experimental and numerical studies of flow over a dimpled plate have been conducted in conjunction with two major flow configurations; *i*) channel flow and *ii*) zero-pressure-gradient boundary layer flow over a flat plate. Kovalenko *et al*.[11] collected and analyzed a substantial amount of experimental results for channel flow with a single dimple for $Re_c \in [500, 100000]$ and for the dimple depth d to dimple diameter D ratio $d/D \in [0.1, 0.5]$, where Re_c denotes the Reynolds number based on D and the centerline velocity U_c. Figure 1 shows the sketch of the dimple geometry. These experimental data were provided from previous works published by (among others) a range of scientists in the former Soviet Union, and later Russia and Ukraine (see Kovalenko *et al*.[11] and the references therein for the detailed publications). More recently detailed flow measurements for laminar incoming boundary layer flow over a single dimple recessed in a flat plate were conducted by Tay *et al.*[12] using dye flow visualization. Here Re_D ranges from 1000 to 28000 while d/D ranges from 0.05 to 0.5 where Re_D denotes the Reynolds number based on D and the freestream velocity U. Two side-by-side dimples, one with a round edge and the other with a sharp edge, were used in their experiments with the distance between them being large enough so that the flow over each dimple was independent of the flow over the other dimple. Tay *et al.*[12] reported six qualitatively different flow patterns, of which four were previously observed by Kovalenko *et al*.[11].

Figure 2 shows a sketch of these six flow patterns. Here flow pattern *I* (figure 2*a*) is characterized by the streamlines first bending towards the streamwise centerline of the dimple (indicated by the red dotted dash line) and then bending away from it; flow pattern *II* (figure 2*b*) is similar to *I* except for the existence of a small flow recirculation region within the upstream part of the

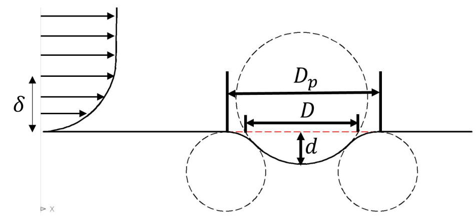

FIG. 1. Sketch of the dimple geometry and the inlet boundary layer flow

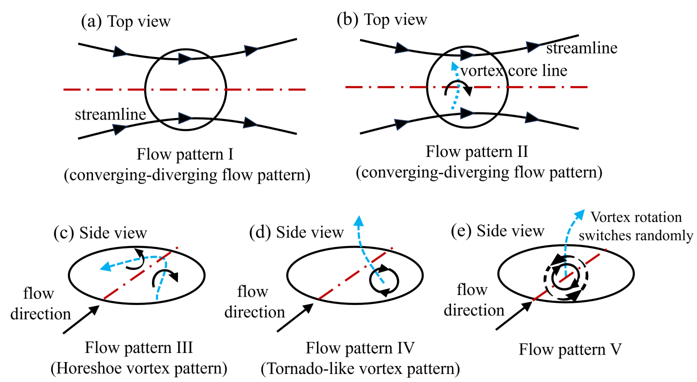

FIG. 2. Sketch of the flow patterns found in the measurements of Tay *et al.*[12]. The red dotted dash line denotes the streamwise centerline of the dimple; the blue dash line represents the vortex core line while the black arrow line around the vortex core line indicates the vortex rotation direction.

dimple as visualized by the vortex core line (indicated by the blue dashed arrow line where the surrounding black arrow line indicates the vortex rotation direction). These two flow patterns are similar to the 'diffuser-confuser' flow pattern classified by Kovalenko *et al*.[11]. More recently, this flow pattern has also been referred to as the 'converging-diverging' flow pattern[10].

Flow pattern *III* (figure 2*c*) consists of a counter-rotating vortex pair (with rotation indicated by the black arrows) with a continuous vortex core line (depicted by the blue dashed arrow line), which is symmetric about the streamwise centerline of the dimple. This flow pattern was previously classified as the horseshoe vortex pattern by Kovalenko *et al*.[11]. This flow pattern was also observed in Large eddy simulations (LES) conducted by Lan, Xie, and Zhang[13] for turbulent boundary layer flow over a single dimple under an adverse pressure gradient, as well as in the

Reynolds-averaged Navier-Stokes (RANS) simulations of Isaev *et al.*[14] who investigated steady-state turbulent channel flow over a single dimple. Flow pattern IV is characterized by that one of the vortices in the counter-rotating vortex pair increases while the other shrinks, thus forming an asymmetric flow pattern with one dominating vortex as illustrated in figure $2(d)$. The core line of this dominating vortex, which is displaced from the streamwise centerline of the dimple (see figure 2*d*), is directed upwards from the dimple bottom with a slight inclination relative to the vertical axis, which remains stable once it is established. Here the location of the dominating vortex can appear on either side of the streamwise centerline through the dimple with opposite rotation direction, for repeated flow realizations. This flow pattern is qualitatively similar to the tornado-like vortex pattern identified by Kovalenko *et al*.[11]. Qualitatively similar tornado-like vortex structures were also observed in unsteady RANS and LES simulations of Turnow *et al.*[15] for turbulent channel flow with a single dimple. They found that the unsteady RANS simulations can only capture the mean tornado-like vortex structure with an orientation of approximately 45^o inclined to the streamwise direction while LES results showed that the vortex core switched orientation approximately $\pm 45^o$ inclined to the streamwise direction. They also reported that the mean turbulent flow within the dimple, obtained by averaging the streamlines over a long time interval, was qualitatively similar to the symmetric horseshoe vortex pattern. It should be noted here that none of these works have visualized the core line of the shrinking vortex. Flow pattern V (figure 2*e*) was only found in the deepest dimple for $d/D = 0.5$. Here only one vortex is observed within the dimple. The vortex core line near the dimple surface is vertical while higher up from the dimple surface, the core line is bent downstream (see figure 2*e*). Moreover, the vortex may switch its rotational direction randomly as illustrated in figure $2(e)$ by the full and dashed black arrow lines surrounding the vortex core line. In flow pattern VI, the flow exhibits a transition to turbulent/chaotic states (not shown here).

Until now, a substantial number of measurements and numerical simulations have been conducted for flow over a single dimple, resulting in the qualitative description of different flow patterns, described above. However, neither existing measurements nor existing numerical simulations have so far provided information on the detailed physical mechanisms underpinning the occurrence and transition between the different observed flow patterns. To fill in a part of this knowledge gap, direct numerical simulations (DNS) are applied to i) provide a more detailed description of these flow patterns; ii) investigate the physical mechanisms underpinning the transition between these flow patterns; iii) investigate the effect of the flat-plate boundary layer thickness on the flow within a given dimple and *iv*) explain the dimple-induced streaks that occur above the recessed dimple. Specifically, direct numerical simulations are conducted for a laminar zero-pressure-gradient boundary layer flow over a shallow dimple with $d/D = 0.05$ recessed in a flat plate for a fixed $Re_D = 20000$; the thickness δ/D of the boundary layer at the inlet ranges from 0.023 to 0.1.

The paper is organized as follows. The problem definition, numerical method, computational domain, and grid convergence study are given in section *II* and the Appendix. The formation of and transition between the different flow patterns within the dimple as δ/D decreases, are discussed in detail in section *III*. The dimple-induced velocity streaks above the dimple and their formation mechanisms are discussed in section *IV*. Conclusions are given in section *V*.

II. PROBLEM DEFINITION AND GOVERNING EQUATIONS

The current paper addresses a zero-pressure-gradient boundary layer flow over a plate with one single dimple as shown in figure 1 for $Re_D = 20000$, corresponding to a value within a range where either the horseshoe vortex or the tornado-like vortex was observed for different dimple depths in the previous experiments. This allows us to investigate the evolution of these two major vortices within the dimple. The dimple depth-to-diameter ratio d/D and the round edge ratio D_p/D are 0.05 and 1.06, respectively. Most of the previous work on this flow configuration has focused on $d/D > 0.1$. The inlet boundary layer flow is defined by the Blasius-like velocity profile (with zero vertical velocity w) corresponding to the boundary layer thickness δ, defined by the distance between the wall and the height where the streamwise velocity is 99% of the free-stream velocity. The values of δ/D range from 0.023 to 0.1, corresponding to the Reynolds number Re_θ based on the momentum thickness ranging from 280 to 64 as well as the Reynolds number Re_x based on the streamwise location ranging from 1.8×10^5 to 2.5×10^4. The choice of δ/D ensures that the flat-plate boundary layer flow remains laminar since the transition Reynolds number Re_x from laminar to turbulent boundary layer flow in a flat plate is about 5×10^5. Here, the incompressible flow with a constant density ρ and kinematic viscosity ν is governed by the three-dimensional Navier–Stokes equations given as

$$\frac{\partial u_i}{\partial x_i} = 0 \tag{1}$$

$$\frac{\partial u_i}{\partial t} + \frac{\partial u_i u_j}{\partial x_j} = -\frac{1}{\rho}\frac{\partial p}{\partial x_i} + \nu \frac{\partial^2 u_i}{\partial x_j \partial x_j} \tag{2}$$

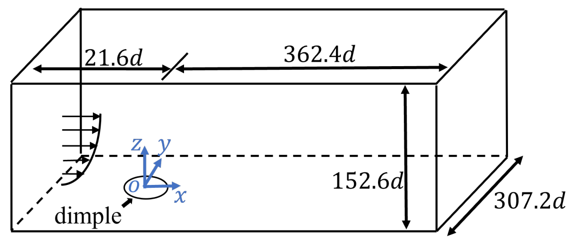

FIG. 3. Sketch of the computational domain

where the Einstein notation using repeated indices is applied. Here $u_i = (u, v, w)$ and $x_i = (x, y, z)$ for $i = 1, 2$, and 3, indicate the velocity and Cartesian coordinates, respectively, while t and p denote the time and pressure, respectively.

A. Numerical methods

The DNS/LES solver MGLET[16,17] utilizing a second-order finite volume method with a staggered grid is used for solving the Navier–Stokes equations. An explicit low-storage third-order Runge-Kutta scheme is used for time integration. The midpoint rule is used to approximate the surface integral of flow variables over the faces of the discrete volumes, and the Poisson equation for pressure correction is solved using Stone's strongly implicit procedure (SIP). The dimple geometry is taken into account by a direct-forcing immersed boundary method, which is described in detail in Peller *et al.*[18]. The code has been thoroughly validated and applied to investigate many complex flows, such as turbulent boundary layer flow over a flat plate[19], turbulent flow in a rod-roughed channel[20], steady and oscillatory flow through a hexagonal sphere pack[21], the spheroid wake[22], the single-step cylinder wake[23] and the curved cylinder wake[24].

B. Computational domain and grid resolution

In the present work, numerical simulations of the zero-pressure-gradient boundary layer flow over the dimpled plate have been conducted for $\delta/D = 0.023$, 0.04, 0.053, 0.069, and 0.1 with $Re_D = 20000$. It should be noted that for a given Re_D, the decrease of δ/D is equivalent to moving the dimple towards the front edge of the plate. Figure 3 shows the computational domain. The inlet and outlet boundaries are located $21.6d$ and $362.4d$ away from the dimple center. The top

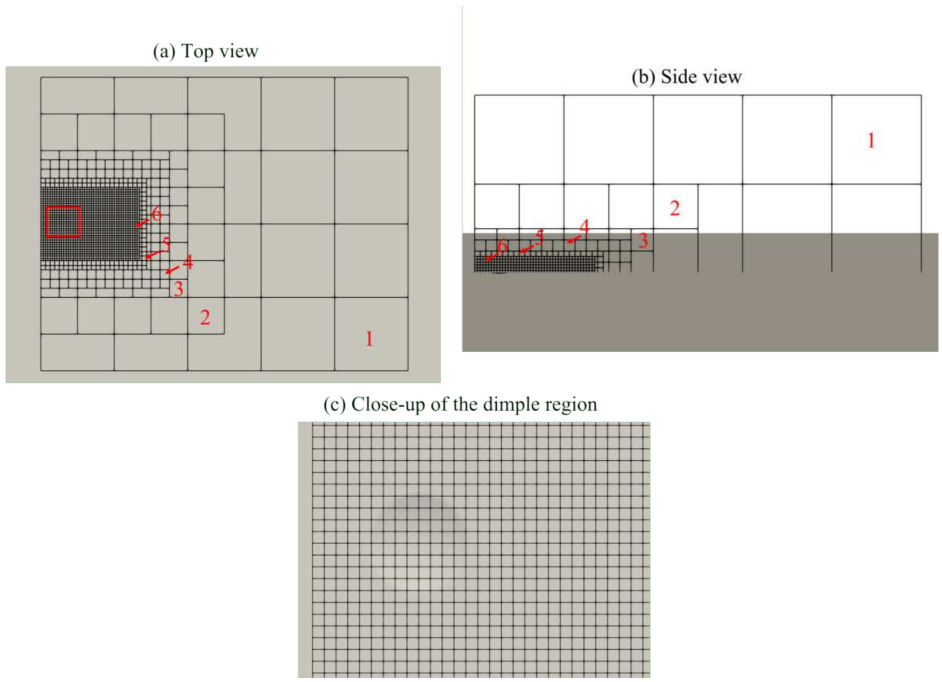

FIG. 4. An illustration of the multi-level grids from the (a) top view and (b) side view; (c) close-up of the grids near the dimple region. The back solid lines denote the edges of a grid box, which contains 40×40×40 cubic grids.

boundary is located 152.6d away from the dimpled plate at the bottom while the boundaries in the spanwise direction are located 307.2d from the dimple center.

A Blasius-like velocity profile with $w = 0$ is applied at the inlet, while a Neumann condition for the velocity ($\partial u_i/\partial x = 0$) and a Dirichlet condition for the pressure ($p = 0$) are imposed at the outlet. At the top boundary, $p = 0$ and $\partial u_i/\partial z = 0$ are imposed in order to ensure a zero pressure gradient condition in the streamwise direction[19]. Slip conditions are used at the side boundaries. Figures 4(a) and 4(b) show the top view and side view of multi-level grids used for the simulations, respectively. The edge length (solid lines) of the cubic grid box is half of that of the grid box at a higher level (marked by red numbers), such as the edge length of the grid box at level 1 being twice as large as at level 2. Moreover, one grid box is composed of 40×40×40 cubic grids. The finest grid, i.e., the level-6 grid box with a grid size of 0.003D is applied over the dimple region as shown in figure 4(c). The present results are all obtained from this level-6 grid region. The total grid number is approximately 0.7 billion. This zonal grid algorithm is described in detail by Manhart[19].

III. FLOW PATTERNS WITHIN THE DIMPLE

In this section, the flow structure within the dimple of $d/D = 0.05$ is presented and discussed for δ/D ranging from 0.023 to 0.1 at $Re_D = 20000$. As δ/D decreases, four different flow patterns are found. The symmetric horseshoe vortex pattern[11,12] depicted in figure 2(c) is observed for $\delta/D \in [0.053, 0.1]$. Two other sub-patterns have been identified within this pattern. These sub-patterns are distinguished by that one pattern consists of a steady asymmetric horseshoe vortex while the other consists of an asymmetric horseshoe vortex exhibiting quasi-periodic movement. Furthermore, a transient flow pattern has been observed between the asymmetric horseshoe vortex pattern and the tornado-like vortex pattern where there is no continuous core line passing through both vortices. The physical mechanisms underpinning the formation of the vortex structures, as well as the transition between the different flow patterns, will be discussed in detail below in subsections *A* to *D*.

A. Horseshoe vortex pattern

Figure 5(a) shows the three-dimensional streamlines (black lines with arrows) and the vortex core line (thick red line) for $\delta/D = 0.1$. Here the vortex core line is calculated from the vorticity vector[25]. The flow is steady and symmetric about the streamwise centerline of the dimple and is spiraling within the dimple, forming a horseshoe vortex as visualized by the vortex core line. This flow pattern is the same as the horseshoe vortex pattern identified by Kovalenko *et al*.[11] from measurements for channel flow over a recessed dimple, and by measurements conducted by Tay *et al.*[12] for laminar flat-plate boundary layer flow over a recessed dimple. The physical mechanisms underpinning the formation of the horseshoe vortex within the dimple will now be discussed thoroughly. In the following discussion, the flow spiral is decomposed into a spanwise flow spiral (i.e., a flow spiral in the *xz*-plane), a vertical flow spiral (i.e., a flow spiral in the *xy*-plane), and a streamwise flow spiral (i.e., a flow spiral in the *yz*-plane), named in accordance with the direction of the relevant vorticity vector component.

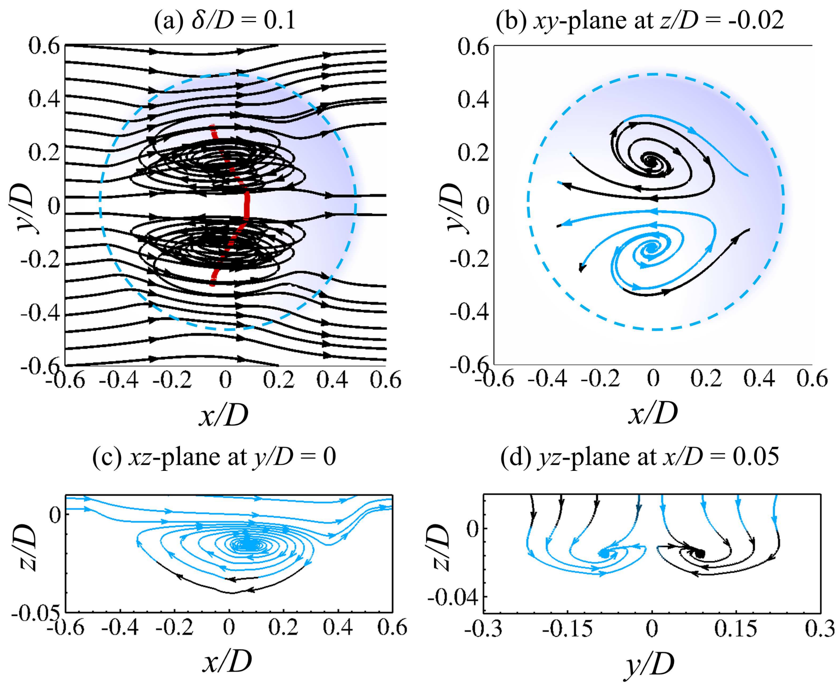

FIG. 5. (a) Three-dimensional ($3D$) streamlines (black lines with arrows) and the vortex core lines (red thick lines); Two-dimensional ($2D$) streamlines in the (b) xy-plane at $z/D = -0.02$, (c) xz-plane at $y/D = 0$ (symmetric plane) and (d) yz-plane at $x/D = 0.05$ for $\delta/D = 0.1$. The blue and black lines denote positive and negative values, respectively, of the relevant vorticity component. The dashed blue line denotes the dimple edge.

Thus, the vertical flow spiral is depicted in figure 5(b), showing the two-dimensional streamlines colored by the vertical vorticity ω_z in the xy-plane at $z/D = -0.02$. The blue and black lines denote positive and negative values, respectively, of the relevant vorticity components. The spanwise flow spiral is illustrated by two-dimensional streamlines colored by the spanwise vorticity ω_y in the xz-plane at $y/D = 0$ shown in figure 5(c), while the streamwise flow spiral is visualized by two-dimensional streamlines colored by the streamwise vorticity ω_x in the yz-plane at $x/D = 0.05$ shown in figure 5(d). Here the locations of these three planes are selected in order to best visualize the flow spiral center corresponding to the vortex core line.

As shown in figure 5(b), the vertical flow spiral induces negative ω_z for $y > 0$ and positive ω_z for $y < 0$. This leads to the vertical component of $\vec{\omega_c}$ along the vortex core line being directed downwards for $y > 0$ and upwards for $y < 0$, thus resulting in a vertically upwards tilting of the vortex core line. This tilting is visualized in figure 6, showing the vorticity vector $\vec{\omega_c}$ along (i.e., tangential to) the vortex core line, where the core line is colored by the vertical location relative to the flat plate where $z/D = 0$. It should be noted that positive ω_z for $y > 0$ and negative ω_z for $y < 0$ (figure 5b) are observed near the dimple surface because of the shear layer formed as the horseshoe vortex approaches the wall.

The spanwise flow spiral (figure 5c) mainly induces negative ω_y near the dimple bottom (since $\partial u/\partial z < 0$ yields the dominating contribution to ω_y at the bottom) and positive ω_y in the central region of the flow spiral, which is consistent with the spanwise component of $\vec{\omega_c}$ being directed towards the positive y-direction in this region (figures 5a and 6). It should be noted that $\vec{\omega_c}$ is nearly parallel to the y-axis near the central part of the dimple.

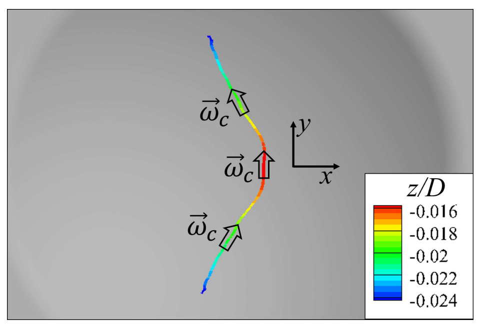

FIG. 6. The top view of the vortex core line.

The streamwise flow spiral in the yz-plane (figure 5d) induces negative ω_x for $y > 0$ and positive ω_x for $y < 0$ near the central region of the flow spiral, causing the downstream tilting of the vortex core line (figure 6); the streamwise component of $\vec{\omega_c}$ is directed towards the negative x-direction for $y > 0$ and towards the positive x-direction for $y < 0$.

Overall, the vortex core line undergoes deformation into a horseshoe shape as a result of the streamwise flow spiral, quantified by ω_x. Therefore, the physical mechanism underpinning the deformation of the vortex core line into the horseshoe shape can be further illustrated by considering the transport equation of ω_x as follows

$$\frac{D\omega_x}{Dt} = \omega_x\frac{\partial u}{\partial x} + \omega_y\frac{\partial u}{\partial y} + \omega_z\frac{\partial u}{\partial z} + Re_D^{-1}\nabla^2\omega_x \tag{3}$$

where the first term on the right-hand side denotes the production of ω_x due to the streamwise stretching or compression of ω_x, while the second and third terms indicate the production of ω_x due to the streamwise tilting of ω_y and ω_z, respectively[26,27]. Here $|\omega_x|$ can only increase if the sign of the production term is the same as the sign of ω_x. Therefore, the increase of ω_x is due to

$$P_{s,x} = \frac{\omega_x}{|\omega_x|}(\omega_x\frac{\partial u}{\partial x}) \tag{4}$$

$$P_{t,y} = \frac{\omega_x}{|\omega_x|}(\omega_y\frac{\partial u}{\partial y}) \tag{5}$$

$$P_{t,z} = \frac{\omega_x}{|\omega_x|}(\omega_z\frac{\partial u}{\partial z}) \tag{6}$$

where $P_{s,x}$, $P_{t,y}$, and $P_{t,z}$ are the net production terms of ω_x caused by the streamwise stretching of ω_x, and the streamwise tilting of ω_y and ω_z, respectively.

Figure $7(a)$ shows the three specific production terms along the vortex core line shown in figure 6 for $\delta/D = 0.1$. The corresponding velocity gradients of u are shown in figure $7(b)$; the vorticity components along the vortex core line are shown in figure $7(c)$. The magnitude of the production term due to streamwise stretching of ω_x, i.e., $P_{s,x}$, (figure 7*a*) is much smaller than the magnitude of the production terms due to the streamwise tilting of ω_y and ω_z, i.e., $P_{t,y}$ and $P_{t,z}$, implying that the streamwise stretching makes a negligible contribution to the production of ω_x. This is mainly due to that $|\frac{\partial u}{\partial x}|$ (figure 7*b*) is very small along the vortex core line.

The production term $P_{t,y}$ (figure 7*a*, showing -$P_{t,y}$) remains negative along the entire vortex core line, implying that the production of ω_x, and thus the deformation of the vortex core line into the horseshoe shape, is counteracted by the streamwise tilting of ω_y. The negative value of $P_{t,y}$ is due to that ω_y (figure 7*c*) remains positive along the vortex core line; ω_x (figure 7*c*) is negative for $y > 0$ and positive for $y < 0$, while $\frac{\partial u}{\partial y}$ (figure 7*b*) is positive for $y > 0$ and negative for $y < 0$ (see Eq.5). It appears that $|P_{t,y}|$ (figure 7*a*) exhibits two maxima; one for $y > 0$ and one for $y < 0$. Here the increase of $|P_{t,y}|$ from $|y| = 0.12$ towards the maxima is caused by the corresponding increase of ω_y (figure 7*c*) due to the strengthening of the spanwise flow spiral towards $y = 0$. Moreover, the decrease of $|P_{t,y}|$ from the maxima towards $y = 0$ is induced by the corresponding decrease of $|\frac{\partial u}{\partial y}|$ (figure 7*b*) due to the weakening of the vertical flow spiral towards $y = 0$.

The production term $P_{t,z}$ (figure 7*a*) remains positive along the vortex core line, implying that the production of ω_x is enhanced by the streamwise tilting of ω_z. Thus the deformation of the

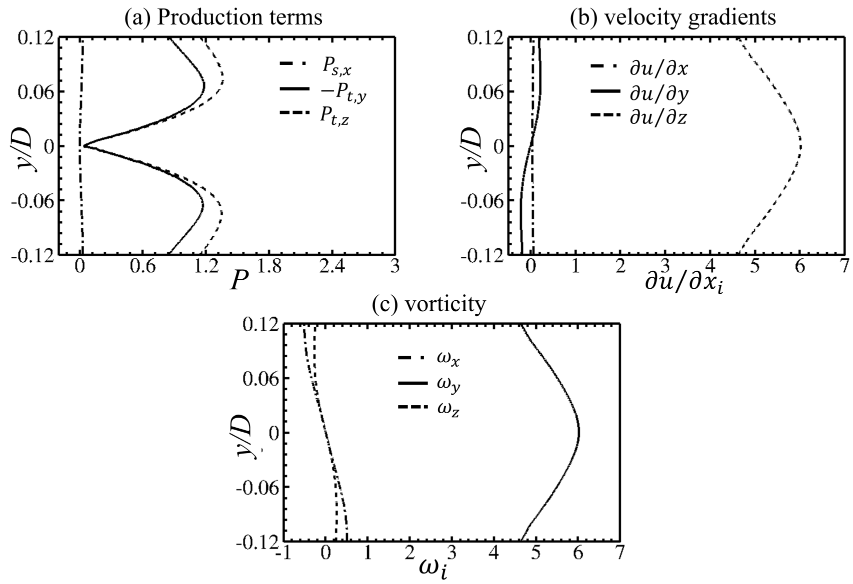

FIG. 7. (a) Production terms of ω_x ($P_{s,x}$, $P_{t,y}$, and $P_{t,z}$), (b) the velocity gradients of u, and (c) the vorticity (ω_x, ω_y, and ω_z) along the vortex core line for $\delta/D = 0.1$.

vortex core line into the horseshoe shape is mainly induced by the streamwise tilting of ω_z, which is consistent with the downstream tilting of the flow spiral. This tilting is mainly induced by the spanwise flow spiral, where $\frac{\partial u}{\partial z} > 0$ along the whole vortex core line as shown in figure $7(b)$. Furthermore, $P_{t,z}$ first increases and then decreases as $|y|$ decreases, qualitatively similar to that observed for $P_{t,y}$. The underpinning mechanism is similar to that for $P_{t,y}$; as $|y|$ decreases, the increase of the local dimple depth strengthens the spanwise flow spiral, leading to an increase of $\frac{\partial u}{\partial z}$ (figure 7*b*) but weakens the vertical flow spiral, thus resulting in a decrease of $|\omega_z|$ (figure 7*c*).

The symmetric horseshoe vortex pattern also occurs for $\delta/D = 0.069$ and 0.053 as illustrated in figure $8(a)$ and $8(b)$, respectively, showing three-dimensional streamlines and the corresponding vortex core lines (red thick line). Figures $8(c)$-$8(d)$ show the vortex core lines for $\delta/D = 0.1, 0.069$ and 0.053 viewed from the top (*xy*-plane) and side (*xz*-plane), respectively. As δ/D decreases, the vertical tilting of the vortex core line (figure 8*d*) remains qualitatively similar while the vortex core line within the central part of the dimple is tilted farther downstream (figure 8*c*), i.e., the head of

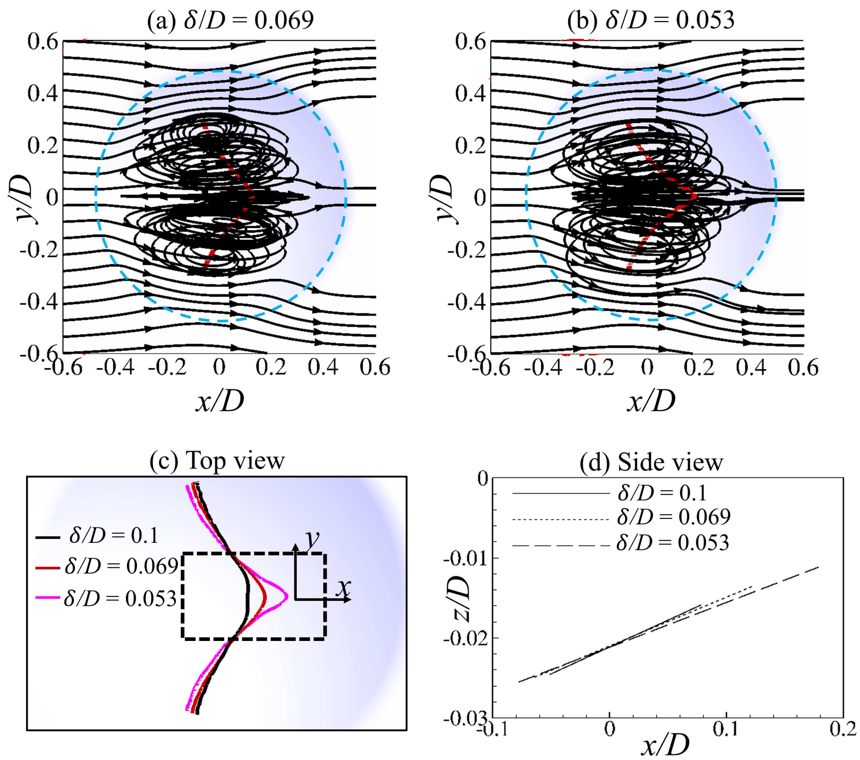

FIG. 8. (a)-(b) Three-dimensional ($3D$) streamline topologies (black lines with arrows) and the vortex core lines (red thick lines) for $\delta/D = 0.069$, and 0.053; (c)-(d) The vortex core lines for $\delta/D = 0.1$, 0.069 and 0.053 from the top and side views. The dashed blue line denotes the dimple edge.

the horseshoe vortex moves farther downstream, forming a sharper shape of the horseshoe vortex. This can be explained by that the streamwise flow spiral within the dimple (and thus ω_x) becomes stronger as δ/D decreases, and this effect is largest near the center of the dimple. The relative importance of the tilting and stretching on the growth of ω_x is assessed by evaluating the ratio P_t/P_{t+s} between the integral values of the tilting terms and the total production term given below

$$P_t = \int_V (P_{t,y} + P_{t,z})\, dV \tag{7}$$

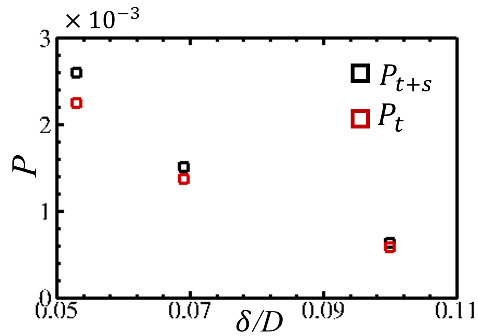

FIG. 9. Integral values of the tilting terms P_t and the total production term P_{t+s} over a control volume V for $\delta/D = 0.053$, 0.069, and 0.1.

$$P_{t+s} = \int_V (P_{t,x} + P_{t,y} + P_{t,z})\, dV \tag{8}$$

where V denotes a control volume ($x/D \in [-0.1, 0.4], y/D \in [-0.2, 0.2], z/D \in [-0.03, 0.0]$) covering the vortex core line with the largest deformation as shown by the box with dashed lines in figure 8(c). The values of P_t and P_{t+s} for $\delta/D = 0.1$, 0.069, and 0.053 are shown in figure 9, illustrating that as δ/D decreases from 0.1 to 0.053, P_t and P_{t+s} increase, while the ratio P_t/P_{t+s} decreases from approximately 93% to 86%. This implies a small increase in the small contribution from the stretching to the production of ω_x.

Overall, the deformation of the vortex core line into the horseshoe form is caused by the streamwise flow spiral, which is quantified by the streamwise vorticity component ω_x. The enhanced production of ω_x is mainly due to the tilting of ω_z, while the tilting of ω_y counteracts this production. Decreasing δ/D from 0.1 to 0.053 leads to a stronger flow spiral, and thus a larger production of ω_x, within the dimple. It appears that this effect is largest at the center of the dimple, which explains the sharper head of the horseshoe vortex as δ/D decreases.

B. Steady asymmetric horseshoe vortex pattern

As δ/D decreases to 0.04, the flow exhibits an unsteady behavior initially, where an asymmetric flow pattern develops and results in a steady flow with an asymmetric horseshoe pattern. In the

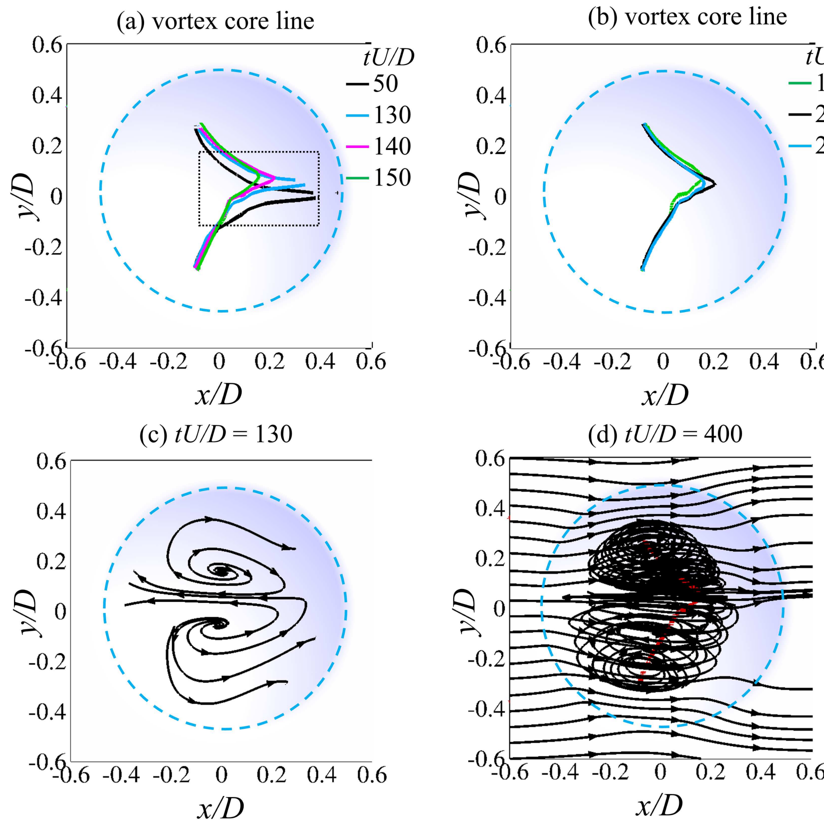

FIG. 10. Instantaneous vortex core lines at (a) $tU/D \in [50,150]$, (b) $tU/D \in [150,250]$; (c) Instantaneous two-dimensional streamlines in the xy-plane at $z/D = -0.02$ for $tU/D = 130$; (d) Instantaneous three-dimensional streamlines at $tU/D = 400$ for $\delta/D = 0.04$. The dashed blue line denotes the dimple edge.

forthcoming, this transient flow development towards the steady asymmetric vortex pattern will be described.

Figures 10(a) and 10(b) show the instantaneous vortex core lines at $tU/D \in [50,250]$. For $tU/D = 50$ (figure 10a), a tornado-like vortex pair is present within the downstream part of the dimple, which can be further visualized by the corresponding ω_x-contours and by two-dimensional streamlines in the yz-plane at $x/D = 0.3$ shown in figure 11(a). The interaction between these

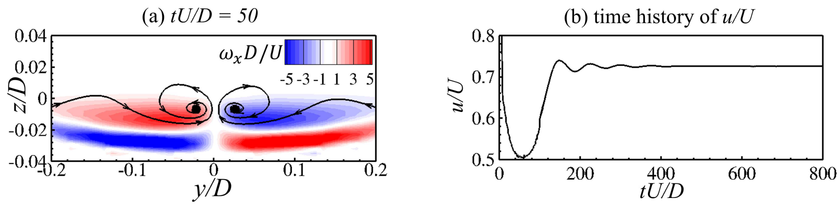

FIG. 11. (a) Two-dimensional streamlines and ω_x-contours in the yz-plane at $x/D = 0.3$; (b) Time history of u probed at $(x/D, y/D, z/D) = (0.5, 0.0, 0.02)$.

two tornado-like vortices appears to induce a flow instability, resulting in a flow asymmetry as visualized by the two-dimensional streamlines in the xy-plane at $z/D = -0.02$ for $tU/D = 130$ in figure $10(c)$. Here the flow spiral region for $y < 0$ (denoted the lower flow spiral region) grows while the flow spiral region for $y > 0$ (denoted the upper flow spiral region) shrinks, leading the vortex pair to move towards the positive y-direction as well as upstream from $tU/D = 50$ to 130 as shown in figure $10(a)$. This flow pattern appears to be qualitatively similar to the tornado-like vortex pattern reported by Kovalenko *et al.*[11] and Tay *et al.*[12], although, in their work, only the dominating vortex core line was depicted. We will refer to this as the tornado-like vortex pair in the forthcoming. At $tU/D = 140$, the vortices within this tornado-like vortex pair connect, forming a horseshoe vortex, of which the head is located at $y > 0$ (pink line in figure 10a). Thereafter, at $tU/D = 150$, the head of the horseshoe vortex moves further upstream. As shown in figure $10(b)$, the head of the horseshoe vortex moves slightly downstream for $tU/D = 200$, and then, at $tU/D = 250$, it moves upstream. This small oscillation of the head's position decays gradually and only lasts for a period of about 400 time units as illustrated by the time history of u probed at the downstream edge of the dimple, i.e., at (x/D, y/D, z/D) = (0.5, 0, 0.02) as shown in figure $11(b)$.

After $tU/D \approx 400$, the flow becomes steady and asymmetric about the streamwise centerline of the dimple as shown in figure $10(d)$, which shows the three-dimensional streamlines and the vortex core line for $tU/D = 400$. It should be noted that the head also moves vertically upwards and downwards as the head moves downstream and upstream, but this vertical displacement is less than 2% of the corresponding streamwise displacement, and will not be further discussed here.

The major mechanism underpinning the deformation of the vortex within the dimple can again

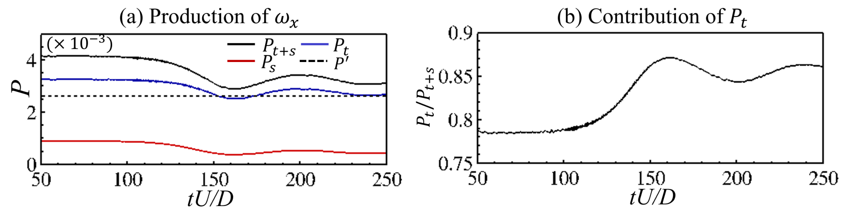

FIG. 12. (a) Time history of the production terms P_{t+s}, P_t, P_s and P'; (b) Time history of the ratio P_t/P_{t+s}.

be explained by the production of ω_x owing to the stretching of ω_x and the tilting of ω_y and ω_z within the dimple as discussed for the symmetric horseshoe vortex pattern in Section *III-A*. Figure 12(a) show the time history of $P_s = \int_V P_{s,x}\, dV$, P_t (Eq.7) and P_{t+s} (Eq.8) for $tU/D \in [50,250]$. Here P' denotes the value of P_{t+s} for $\delta/D = 0.053$, which is taken as a reference. The area of the control volume V is shown by the box with dashed lines in figure 10(a). From $tU/D = 50$ to 130, P_{t+s} for $\delta/D = 0.04$ is larger than that for $\delta/D = 0.053$ (represented by $P^{'}$), showing a larger production of the streamwise vorticity ω_x for $\delta/D = 0.04$ than for $\delta/D = 0.053$, leading to the formation of the tornado-like vortex pair. Then, from $tU/D = 130$ to 160, P_{t+s} decreases significantly, implying a decrease in the production of ω_x, resulting in the connection of vortices within the tornado-like vortex pair, thus forming a horseshoe vortex (figure 10a, pink line). Subsequently, P_{t+s} starts to increase again but reaches a smaller maximum value than before. The flow pattern remains a horseshoe vortex where the head moves slightly downstream from $tU/D = 150$ to 200 as shown in figure 10(b). Thereafter, P_{t+s} decreases as the head moves upstream from $tU/D = 200$ to 250 (figure 10b). This slight upstream and downstream movement of the horseshoe vortex head continues for an intermediate period and finally reaches a steady state as shown by the time-history of streamwise velocity u/U in figure 11(b). Moreover, as shown in figure 12(a), the trend of P_{t+s} is almost the same as for P_t, which is larger than P_s, again implying that the tilting of ω_y and ω_z yields the dominating contribution to the production of ω_x, which leads to the deformation of the vortex within the dimple.

The relative importance of the tilting and stretching can be further quantified by the time history of the ratio P_t/P_{t+s} as shown in figure 12(b) for $tU/D \in [50,250]$. For $tU/D \in [50,100]$, the contribution from the tilting (P_t/P_{t+s}) is approximately 78% when the tornado-like vortex pair is located at the central part of the dimple (figure 10a). Then, P_t/P_{t+s} increases to the maximum

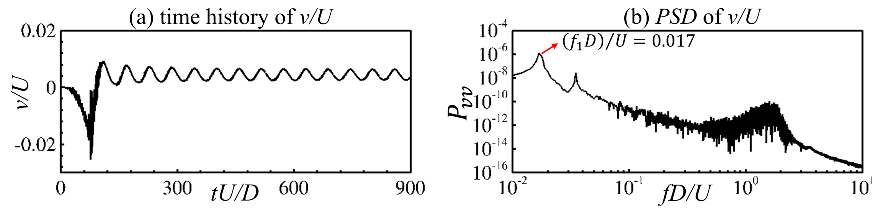

FIG. 13. (a) Time history of v/U probed at $(x/D, y/D, z/D) = (0.5, 0.0, 0.02)$ for $\delta/D = 0.033$; (b) Power spectral density (PSD) of v/U for $\delta/D = 0.033$.

value of approximately 87% from $tU/D = 100$ to 150 when the vortex pair starts to move towards the positive y direction and connect, forming the horseshoe vortex (figure 10a). A decrease of P_t/P_{t+s} from $tU/D = 150$ to 200 and an increase of P_t/P_{t+s} from $tU/D = 200$ to 250 are observed, coinciding with the downstream and upstream movements of the horseshoe vortex (figure 10b), respectively. Finally, P_t/P_{t+s} remains approximately 86% as the flow becomes steady.

C. Quasi-periodic asymmetric horseshoe vortex pattern

As δ/D decreases to 0.033, the flow exhibits qualitatively similar behavior as the steady asymmetric pattern discussed above; the flow structure within the dimple initially develops into a tornado-like vortex pair (see, e.g., figure 10a for $tU/D = 50$), and then these two tornado-like vortices connect, forming a horseshoe vortex (see, e.g., figure 10a for $tU/D = 140$). It should be noted that here the head of the horseshoe vortex keeps moving quasi-periodically within the dimple, i.e., there is no steady state. The flow periodicity is clearly illustrated by the oscillation of v/U probed at $(x/D, y/D, z/D) = (0.5, 0, 0.02)$ shown in figure 13(a). A mean value of v/U larger than zero implies that the flow is asymmetric about the streamwise centerline of the dimple where the flow spiral region grows for $y < 0$ and shrinks for $y > 0$, i.e., the head of the horseshoe vortex moves upstream and towards the positive y-direction. Furthermore, the oscillation frequency (f_1D/U) is 0.017 as shown by the power spectral density (PSD) of v/U in figure 13(b).

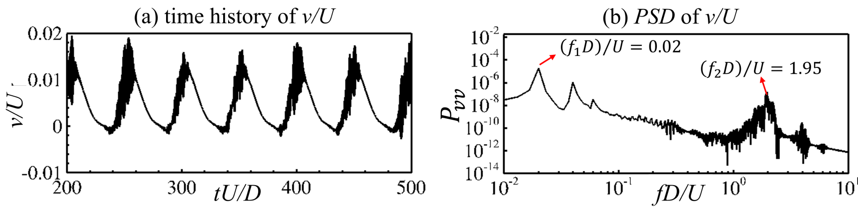

FIG. 14. (a) Time history of v/U probed at $(x/D, y/D, z/D) = (0.5, 0.0, 0.02)$ and (b) Power spectral density (PSD) of v/U for $\delta/D = 0.023$.

D. Mixed horseshoe and tornado-like vortex pattern

As δ/D decreases to 0.023, the flow becomes more unsteady than for $\delta/D = 0.033$. This can be clearly visualized by the time-history of v/U probed at (x/D, y/D, z/D) = (0.5, 0, 0.02) for $\delta/D = 0.023$ in figure 14(a), where the fluctuation of v/U is clearly visible when v/U increases, e.g., from $tU/D = 340$ to 360. The corresponding vortex core lines are shown in figure 15(a). A tornado-like vortex pair is present for $tU/D = 340$ and then moves upstream as well as towards the positive y-direction from $tU/D = 350$ to 360. This behavior is qualitatively similar to that for the initial flow development in the steady asymmetric pattern (figure 10a) as well as the quasi-periodic asymmetric pattern, i.e., the formation of the tornado-like vortex pair. As the vortex pair connect with each other for $tU/D = 370$ (figure 15b), forming a horseshoe vortex, the fluctuation of v/U vanishes (figure 14a). This indicates that the fluctuation within the oscillation of v/U is mainly induced by the interaction between vortices within the tornado-like vortex pair (figure 15a). Then, for $tU/D = 380$), the head of the horseshoe vortex moves downstream and towards the negative y-direction, and the horseshoe vortex evolves into a tornado-like vortex pair again, coinciding with the corresponding fluctuation of v/U observed in figure 14(a). This behavior repeats itself quasi-periodically with alternating formations of tornado-like and horseshoe vortices; this represents a mixed horseshoe and tornado-like vortex pattern. Moreover, figure 14(b) depicts the power spectrum density of v/U, showing that the tornado-like vortex pair or horseshoe vortex within the dimple oscillates with a frequency (f_1D/U) of 0.02 which is higher than for $\delta/D = 0.033$ (where $f_1D/U = 0.017$), while the interaction between the vortices within the tornado-like vortex pair induces a disturbance with a band of high frequencies with a peak frequency (f_2D/U) of 1.95.

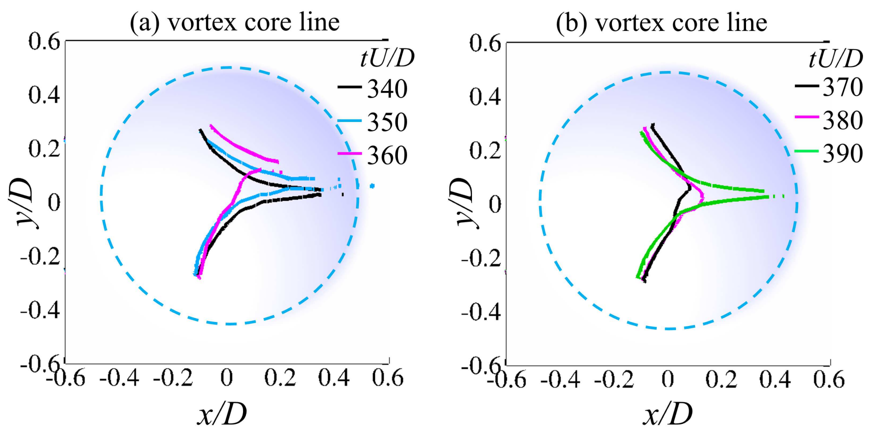

FIG. 15. The instantaneous vortex core lines for $\delta/D = 0.023$ (a) from $tU/D = 340$ to 360 and (b) from $tU/D = 370$ to 390. The dashed blue line denotes the dimple edge.

Overall, a decrease of δ/D from 0.1 to 0.023 leads to increased net production of ω_x, which leads to a transition between four different flow patterns; *i*) the symmetric horseshoe vortex pattern observed for $\delta/D \in [0.1, 0.053]$ where the flow is steady and symmetric about the streamwise centerline of the dimple; *ii*) the steady asymmetric horseshoe vortex pattern observed for $\delta/D = 0.04$ where the flow asymmetry appears to be induced by a flow instability mechanism within a tornado-like vortex pair; *iii*) the quasi-periodic asymmetric horseshoe vortex pattern observed for $\delta/D = 0.033$ where the head of the horseshoe vortex within the dimple moves slightly upstream and downstream quasi-periodically; *iv*) the mixed horseshoe and tornado-like vortex pattern observed for $\delta/D = 0.023$ where the flow within the dimple alternates between the tornado-like vortex pair and the horseshoe vortex in a quasi-periodic manner. Moreover, the first frequency (f_1D/U) increases while the secondary frequency (f_2D/U) becomes visible as δ/D decreases from 0.04 to 0.023. Hence it is reasonable for us to assume that a decrease of δ/D for a given dimple depth is qualitatively equivalent to an increase of the dimple depth for a given δ/D, which might enhance these two frequencies. However, further work is required to confirm this assumption, which is outside the scope of the present work.

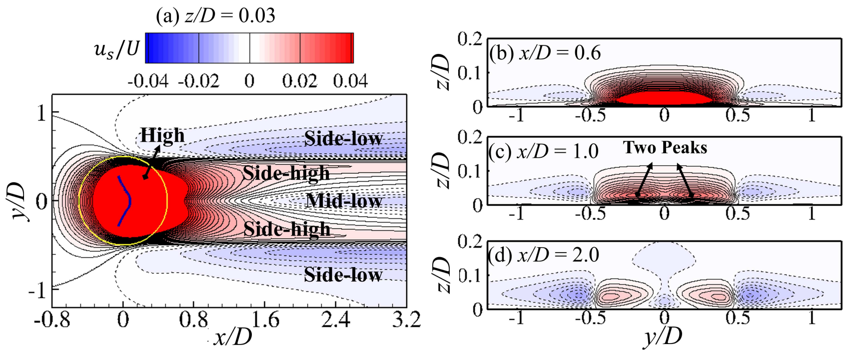

FIG. 16. The streak velocity (u_s/U) contours for $\delta/D = 0.1$ in the (a) xy-plane at $z/D = 0.03$, in the yz-plane at $(b)x/D = 0.6$, $(c)1.0$ and $(d)2.0$. The black solid and dashed lines represent the positive and negative values of u_s/U, respectively. The yellow line denotes the dimple edge, and the dark blue solid line indicates the vortex core line within the dimple region.

IV. DIMPLE-INDUCED STREAKS ABOVE A DIMPLE

In this section, the dimple-induced velocity streaks for different flow patterns are presented and discussed for δ/D ranging from 0.023 to 0.1 at $Re_D = 20000$. Here the velocity streaks are depicted by the contours of $u_s/U = (u - u_0)/U$, i.e., by the normalized deviation from the streamwise velocity u_0 of a zero-pressure-gradient boundary layer flow over a flat plate[27], which is obtained from the present numerical simulations using the same grid resolution as applied for the dimpled plate. Here the streaks represent a deformation of the streamwise velocity induced by the dimple, affecting the laminar flat-plate boundary layer flow.

A. Symmetric pattern

The velocity streaks induced by the dimple mainly consist of four different streaks as depicted in figure 16(a), showing the contours of u_s/U in the xy-plane at $z/D = 0.03$ for the symmetric pattern at $\delta/D = 0.1$. These are i) a High-speed streak region ($u_s > 0$, marked as High) above the dimple and in the near-wake region; ii) two Side-low-speed streak ($u_s < 0$, marked as Side-low) located outside the span of the dimple ($y/D < -0.5$ and $y/D > 0.5$); iii) two Side-high-speed

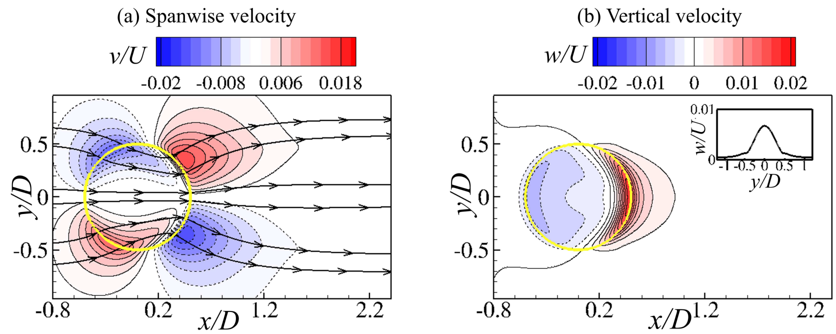

FIG. 17. (a) The spanwise velocity (v/U) contours and the vertical velocity (w/U) contours for $\delta/D = 0.1$ in the xy-plane at $z/D = 0.03$, where the black solid and dashed lines represent the positive and negative values, respectively. The yellow line denotes the dimple edge.

streaks ($u_s > 0$, marked as Side-high) and iv) a Mid-low-speed streak ($u_s < 0$, marked as Mid-low) formed farther downstream at $x/D \approx 1.6$. The mechanisms underpinning the formation of these streaks are now further discussed.

The High-speed streak region (figure 16a) is caused by the flow velocity at a given vertical position of $z > 0$ being located farther away from the dimple surface (located at $z < 0$) than from the corresponding flat plate (located at $z = 0$), thus leading to a larger flow velocity above the dimple (for $z > 0$) than above the flat plate, due to less friction. This represents an acceleration of the streamwise velocity u caused by the dimple, which is here denoted the flow acceleration effect. This High-speed streak ('High') is located within the span of the dimple at $y/D \in [-0.5, 0.5]$.

Two Side-low-speed streaks ($u_s < 0$, marked as Side-low) are formed outside the span of the dimple ($y/D < -0.5$ and $y/D > 0.5$); this is further illustrated by the u_s/U contours in the yz-plane at $x/D = 0.6$ in figure 16(b). The formation of the Side-low-speed streaks can be explained by the v/U contours and the two-dimensional streamlines in the xy-plane at $z/D = 0.03$ which are both shown in figure 17(a). In order to better visualize the curvature of the streamlines, the values of v/U are here amplified by a factor of 20 while the contours of v/U are not scaled. It appears that this flow exhibits the behavior of a confuser-diffuser flow[11] as the streamlines (from the left towards the right) first bend towards the streamwise centerline of the dimple and then bend away from it. The presence of the dimple-induced spanwise velocity v leads to a decrease of u in the

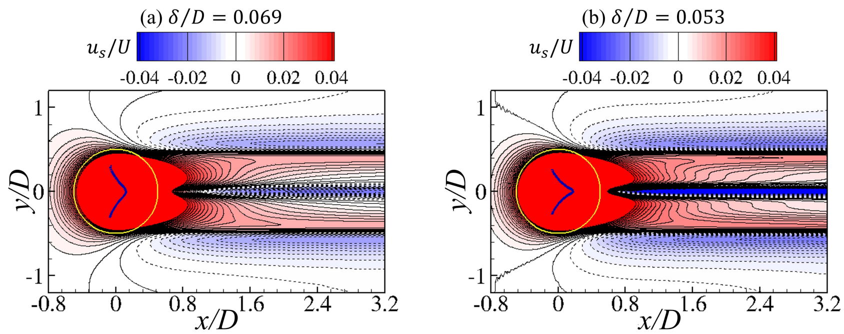

FIG. 18. The streak velocity (u_s/U) contours in the xy-plane at $z/D = 0.01$ for $\delta/D = (a)$ 0.069 and (b) 0.053, where the black solid and dashed lines represent the positive and negative values of u_s/U, respectively. The yellow line denotes the dimple edge, and the dark blue solid line indicates the vortex core line within the dimple region.

'Side-low' region marked in figure 16(a), relative to the corresponding streamwise velocity u_0 over the flat plate. It should be noted that this decrease (caused by the diffuser effect) counteracts the increase of u induced by the flow acceleration effect in the 'High' region. Thus, the gradual growth of the Side-low-speed streak regions farther downstream is mainly caused by a dynamic balance between the diffuser effect and the flow acceleration effect. It appears that the Side-low-speed streaks are less affected by the dimple-induced vertical velocity w than the dimple-induced spanwise velocity v as illustrated in figure 17(b), showing the w/U-contours in the xy-plane at $z/D = 0.03$; the induced vertical velocity w is contained within the span of the dimple.

The High-speed streak becomes weaker farther downstream (figure 16a) due to the absence of the flow acceleration effect since the region downstream of the dimple consists of a flat plate. At $x/D \approx 1.6$, the High-speed streak splits into two Side-high-speed streaks (marked as Side-high) as the Mid-low-speed streak (marked as Mid-low) is formed in-between as further illustrated by the u_s/U contours in yz-plane at $x/D = 1.0$ and 2.0 in figure 16(c)-16(d). This is mainly caused by the local depth variation of the dimple and the horseshoe vortex (the vortex core line is marked as a solid blue line in figure 16a) within the dimple. As the local depth of the dimple increases from the spanwise sides of the dimple towards the centerline $y = 0$, the flow acceleration effect becomes stronger due to less friction, leading to an increase of u_s/U as $|y|$ approaches 0. However,

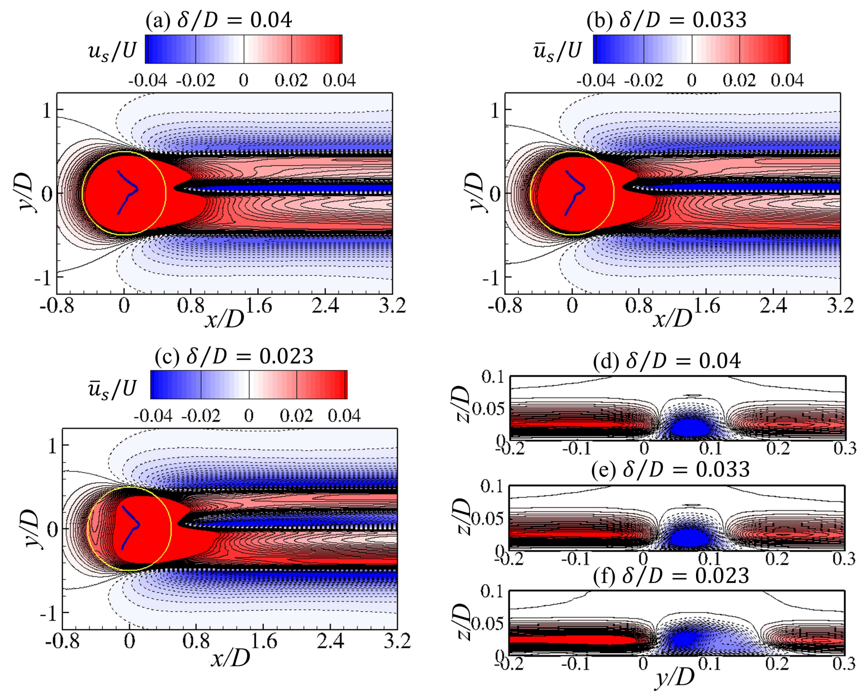

FIG. 19. The streak velocity (u_s/U) contours for $\delta/D = (a)$ 0.04 and the time-averaged $\bar{u}_s/U$ contours for $\delta/D = (b)$ 0.033, and (c) 0.023 in the xy-plane at $z/D = 0.01$, where the black solid and dashed lines represent the positive and negative values of u_s/U, respectively. The yellow line denotes the dimple edge, and the dark blue solid line within the dimple region indicates the vortex core line. (d)-(f) show the corresponding u_s/U or $\bar{u}_s/U$ contours in the yz-plane at $x/D = 1.0$ for $\delta/D = 0.04$, 0.033, and 0.023, respectively.

the strengthening of the spanwise flow spiral towards the head of the horseshoe vortex results in an increase of w/U towards $y = 0$ as illustrated in the top-right frame of figure 17(b), showing w/U along the spanwise direction at $(x/D, z/D) = (0.6, 0.03)$. Here the vertical velocity induces a 'lift-up' mechanism[28], which displaces low-momentum fluid away from the wall, thus tilting the boundary layer upwards, leading to a decrease of u for a given z/D. The value of u_s/U first increases (due to stronger flow acceleration effect) and then decreases (due to stronger 'lift-up'

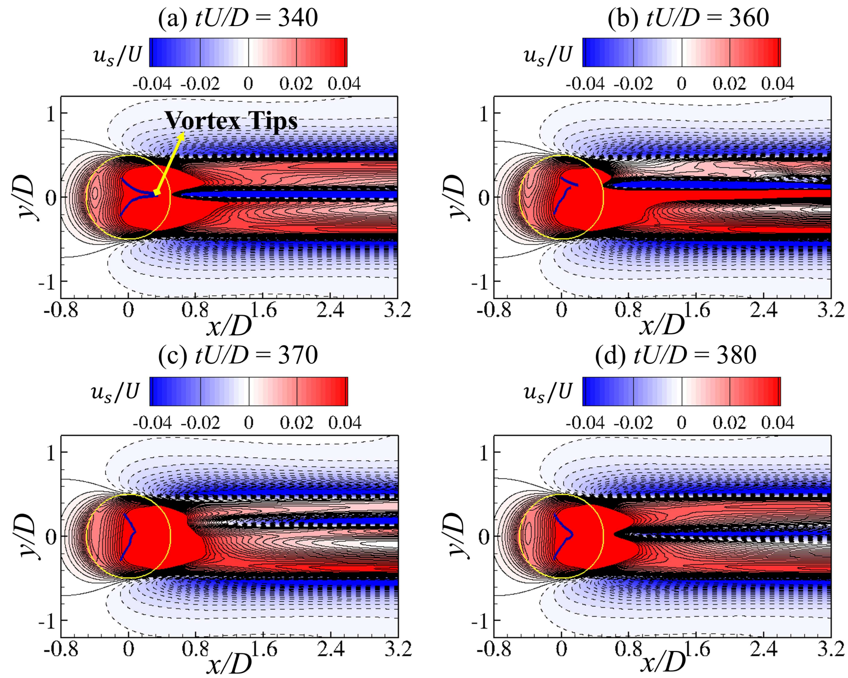

FIG. 20. The instantaneous streak velocity (u_s/U) contours for $\delta/D = 0.023$ at $tU/D = (a)$ 340, (b) 360, (c) 370, and (d) 380 in the xy-plane at $z/D = 0.03$, where the black solid and dashed lines represent the positive and negative values of u_s/U, respectively. The yellow line denotes the dimple edge, and the dark blue solid line indicates the vortex core line within the dimple region.

mechanism) from the dimple sides towards $y = 0$, leading to the formation of the Side-high-speed streaks and the Mid-low-speed streak in-between.

Now the effect of δ/D on the velocity streaks is further investigated for the symmetric pattern. Figures 18(a) and 18(b) show the contours of u_s/U in the xy-plane at $z/D = 0.03$ for $\delta/D =$ 0.069 and 0.053, respectively. As δ/D decreases, all velocity streaks become stronger because a decrease of δ/D implies an increase of the flow velocity at a given vertical position over the dimple, resulting in a stronger flow spiral, as discussed previously (figure 8), thus strengthening both the diffuser effect and the 'lift-up' mechanism as well as the flow acceleration effect. It should be noted that the Mid-low-speed streak is located closer to the dimple as δ/D decreases due to a shift in the balance between the 'lift-up' mechanism and the flow acceleration effect. Moreover, the spanwise location of the Mid-low-speed streak always coincides with the head of the horseshoe vortex where the dominating spanwise flow spiral leads to a stronger 'lift-up' mechanism towards the horizontal line through the horseshoe vortex head. This behavior is also found in the steady and quasi-periodic asymmetric patterns discussed below.

B. Steady and quasi-periodic asymmetric patterns

Figure 19 shows the u_s/U contours for the steady asymmetric pattern at $\delta/D = 0.04$, as well as the time-averaged streak velocity $\overline{u}_s/U$ contours for the quasi-periodic asymmetric pattern, at $\delta/D = 0.04$, 0.033 and 0.023 in the xy-plane at $z/D = 0.03$. The high- and low-speed streaks are here asymmetric about the streamwise centerline of the dimple; the High-speed streak located at $y < 0$ covers a larger region in the dimple wake than that located at $y > 0$. The spanwise location of the Mid-low-speed streak remains the same as that of the horseshoe vortex head for all these cases. Moreover, the velocity streak contours are quite similar for $\delta/D = 0.04$ and 0.033 (figure 19a and 19b). However, the Mid-low-speed streak for $\delta/D = 0.023$ (figure 19c) diffuses in the spanwise direction, becoming wider and weaker than those for $\delta/D = 0.04$ and 0.033 as shown by the corresponding streak velocity contours in the yz-plane at $x/D = 1.0$ in figures 19(d)-19(f). This behavior will now be further explained by the instantaneous streak velocity contours for $\delta/D = 0.023$ shown in figure 20 for $tU/D \in [340, 380]$. The corresponding evolution of the vortex core line within the dimple was previously discussed in section D (figure 15)

For $tU/D = 340$ (figure 20a), the tornado-like vortex pair (the two dark blue solid vortex core lines) within the dimple, which is also clearly shown in figure 15(a), is slightly asymmetric about the streamwise centerline of the dimple. The spanwise location of the Mid-low-speed streak coincides with the horizontal line between the two tips of the vortex pair. Thus, the velocity streaks are asymmetric about the horizontal dimple centerline where the High-speed streak located at $y < 0$ is slightly larger than that located at $y > 0$. It should be noted that here the 'lift-up' mechanism can also be induced by the tornado-like vortex pair as discussed in Brandt and Henningson[29], but, in the present case, this effect is much weaker than that induced by the spanwise flow spiral. Then, for $tU/D = 360$ (figure 20b), the tornado-like vortex pair moves towards the positive y direction, leading to the corresponding movement of the Mid-low-speed streak, thus resulting in a more asymmetric streak pattern than that for $tU/D = 340$; the Side-low-speed streak located at $y > 0$

is much weaker and smaller than that located at $y < 0$. This is mainly because the flow acceleration effect for $y > 0$ is counteracted by the 'lift-up' mechanism (which is strongest between the two tips of the vortex pair) and strongly weakened by the friction due to the decrease of the local depth within the dimple towards the dimple side. Thereafter, for $tU/D = 370$ (figure 20*c*), the connection of vortices within the tornado-like vortex pair forms a horseshoe vortex, which moves upstream; the spanwise flow spiral (figure 15) becomes weaker, causing a weaker 'lift-up' mechanism, thus leading to the decay and downstream movement of the Mid-low-speed streak. As the head of the horseshoe vortex moves towards the centerline $y = 0$ and downstream for $tU/D = 380$ (figure 20*d*), the velocity streaks become nearly symmetric again while the Mid-low-speed streak grows and moves closer to the dimple. Overall, the Mid-low-speed streak is widened by the spanwise movement of the vortex pair (or by the horseshoe vortex) and weakened by the upstream movement of the horseshoe vortex.

Overall, there are three major mechanisms underpinning the formation and evolution of the dimple-induced velocity streaks; *i*) the flow acceleration effect, which induces a larger u above the dimple (for $z > 0$) than above a flat plate; *ii*) the flow diffuser effect, which induces a spanwise velocity in the dimple wake, resulting in a decrease of u; *iii*) the 'lift-up' mechanism, which induces a vertical velocity w, thus leading to a decrease of u at a given vertical position.

V. SUMMARY AND CONCLUSION

In the present work, numerical investigations of a laminar zero-pressure-gradient boundary layer flow over a single shallow dimple recessed in a flat plate have been conducted for $Re_D = 20000$ and $d/D = 0.05$ with $\delta/D \in [0.023, 0.1]$. The flow patterns consist of a transient connection between the horseshoe vortex pattern and the tornado-like vortex pattern as shown in figure 2(c) and 2(d), respectively. Here the horseshoe vortex is characterized by a continuous vortex core line through the two flow spirals within the dimple, while this core line is not continuous for the tornado-like vortex. This is consistent with the previous qualitative description of these vortex patterns (based on measurements) by Kovalenko *et al.*[11] and Tay *et al.*[12], although they did not present the vortex core line. Moreover, the physical mechanisms underpinning the vortex formation and deformation as well as the transition between the different flow patterns have been visualized and discussed. The dimple-induced streak patterns and the mechanisms underpinning their formation and evolution have also been analyzed in detail.

TABLE I. Four flow patterns and the corresponding characteristics for laminar boundary layer flow over a shallow dimple with $d/D = 0.05$ for δ/D ranging from 0.023 to 0.1 at $Re_D = 20000$.

δ/D	Pattern	Characteristic of each pattern
0.1-0.053	Symmetric horseshoe vortex pattern	A steady and symmetric horseshoe vortex, of which core line is tilted farther downstream with decreased δ/D.
0.040	Steady asymmetric horseshoe vortex pattern	A steady and asymmetric horseshoe vortex.
0.033	Quasi-periodic asymmetric horseshoe vortex pattern	An asymmetric horseshoe vortex, where the head moves quasi-periodically within the dimple.
0.023	Mixed horseshoe and tornado-like vortex pattern	An alternating formation of a horseshoe vortex and a tornado-like vortex pair.

The results show that as δ/D decreases from 0.1 to 0.023 for $Re_D = 20000$, the flow with the single dimple exhibits a transition sequence between four different flow patterns as summarized in Table I; *i*) a symmetric horseshoe vortex pattern for $\delta/D \in [0.053, 0.1]$, where the horseshoe vortex is formed within the dimple with the head located farther downstream as δ/D decreases; *ii*) a steady asymmetric horseshoe vortex pattern for $\delta/D = 0.04$, where an asymmetric horseshoe vortex is formed within the dimple; *iii*) a quasi-periodic asymmetric horseshoe vortex pattern for $\delta/D = 0.033$, where the head of the asymmetric horseshoe vortex exhibits small oscillation within the dimple; *iv*) a mixed horseshoe and tornado-like vortex pattern for $\delta/D = 0.023$, characterized by the alternating formation of a horseshoe vortex and a tornado-like vortex pair (tornado-like vortex pair).

The deformation of the vortex core line into the horseshoe shape is mainly caused by the streamwise flow spiral, quantified by streamwise vorticity component ω_x. The enhancement of ω_x is mainly due to the tilting of the vertical vorticity component ω_z. A decrease of δ/D from 0.1 to 0.053 leads to a stronger flow spiral, and thus an enhancement of ω_x within the dimple. This effect appears to be largest at the center of the dimple, thus explaining the sharper head of the horseshoe vortex as δ/D decreases. As δ/D decreases to 0.04, the interaction between the two tornado-like vortices appears to induce a flow instability, which results in an asymmetric steady horseshoe vortex relative to the streamwise centerline of the dimple. An even further growth of ω_x for $\delta/D = 0.023$ leads to a quasi-periodic alternation between the horseshoe vortex and the tornado-like vortex pair.

There are four different dimple-induced velocity streaks above the dimple; i) a High-speed streak above the dimple caused by a flow acceleration effect due to less friction over the dimple than over the flat plate for a given $z/D > 0$; ii) two Side-low-speed streaks located outside the span of the dimple induced by the flow diffuser effect in the downstream part of the dimple, where the streamline is bent away from the streamwise centerline of the dimple; iii) two Side-high-speed streaks and iv) one Mid-low-speed streak in-between the two Side-high-speed streaks. These high- and low-speed streaks are mainly caused by a dynamic balance between a stronger flow acceleration over the dimple and a stronger 'lift-up' mechanism (which tilts the boundary layer upwards) from the dimple sides towards the streamwise line through the vortex head.

The velocity streaks above the dimple are symmetric about the streamwise centerline of the dimple for $\delta/D \in [0.053, 0.1]$, while for $\delta/D \in [0.023, 0.04]$, the velocity streaks become asymmetric where the Side-high-speed streak located at $y > 0$ is narrower and weaker than its counterpart located at $y < 0$. It should be noted that the spanwise location of the Mid-low-speed streak always coincides with the streamwise line through the vortex head or between the tips of the tornado-like vortex pair. This Mid-low-speed streak moves upstream as δ/D decreases due to the stronger 'lift-up' mechanism. Moreover, the Mid-low-speed streak is widened by the spanwise movement of the tornado-like vortex pair (or the horseshoe vortex) and weakened by the upstream movement of the horseshoe vortex.

ACKNOWLEDGMENTS

We gratefully acknowledge the support for this research from the Department of Marine Technology, Norwegian University of Science and Technology, and the Norwegian Research Council, Grant number 308745. Computing resources were provided by Sigma2 in Norway under the project nn9352k.

DATA AVAILABILITY STATEMENT

The data that support the findings of this study are available from the corresponding author upon reasonable request.

TABLE II. Four flow patterns and the corresponding characteristics for laminar boundary layer flow over a shallow dimple with $d/D = 0.05$ for $\delta/D = 0.023$ at $Re_D = 20000$.

Case	L_x/D	L_y/D	L_z/D	Δ_c/D	f_1D/U ($\pm$0.0025)	f_2D/U ($\pm$0.0025)
M1, Coarse	19.2	15.26	7.63	0.004	0.02	1.95
M1, Medium	19.2	15.26	7.63	0.003	0.02	1.95
M1, Fine	19.2	15.26	7.63	0.0025	0.02	1.95
M2, Medium	26.88	23.04	11.78	0.003	0.02	1.95

Appendix A: Computational domain and grid convergence study

In this section, computational domain and grid convergence studies have been conducted for the zero-pressure-gradient boundary layer flow over the dimpled plate for $Re_D = 20000$ with $\delta/D = 0.023$. A cubic grid is applied over the dimple as shown in figure 4. As shown in table II, three different grid resolutions, i.e., the coarse ($\Delta_c/D = 0.004$), medium ($\Delta_c/D = 0.003$), and fine ($\Delta_c/D = 0.0025$) grid resolutions have been used to investigate the grid convergence within the computational domain (M1) of (L_x/D, L_y/D, L_z/D) = (19.2, 15.26, 7.63), where Δ_c is the grid size for the level-6 grid region, while L_x, L_y and L_z denote the streamwise, spanwise, and vertical lengths of the computational domain, respectively. Another computational domain (M2) which is 1.5 times larger than domain M1 in all directions with the medium grid resolution has been utilized for the domain convergence study.

Table II also shows the two dominating frequencies f_1 and f_2 corresponding to the vortex dynamics within the dimple and the interaction between the two tornado-like vortices, respectively. These two frequencies remain the same for all cases given in table II. Figure 21 shows the comparison of the time-averaged streamwise velocity $\bar{u}/U$ along z/D at $y = 0$ within the dimple at $x/D = -0.3$ (black), 0.0 (red) and 0.3 (light blue) and within the dimple wake at $x/D = 1.0$ (dark blue), 2.0 (green) and 3.0 (pink) obtained by the three different grid resolutions (Coarse, Medium and Fine) and the two different computational domains (M1, M2). These time-averaged values are obtained from the data with 400 time units (D/U) after the flow is fully developed. The results obtained by the fine and medium grid resolutions (using the domain M1) show a good agreement while a small deviation can be observed for the coarse grid resolution (using the domain M1) at,

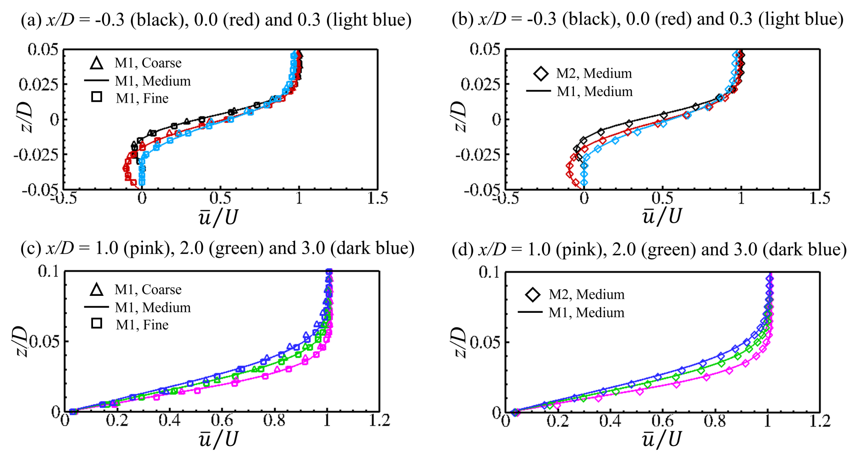

FIG. 21. The time-averaged streamwise velocity $\bar{u}/U$ profile along z at $y = 0.0$ for three different grid resolutions (Coarse, Medium, and Fine) and two different computational domains (M1, M2) sampled (a)-(b) within the dimple at $x/D = -0.3$ (black), 0.0 (red), and 0.3 (light blue), as well as (c)-(d) within the downstream region at $x/D = 1.0$ (pink), 2.0 (green), and 3.0 (dark blue).

e.g., $x/D = 0.3$ and $x/D = 1.0$ as shown in figure 21(a) and 21(c), respectively. A good agreement is also obtained for the results obtained by the two different computational domains using the medium grid resolution as shown in figure 21(b) and 21(d). Furthermore, we have observed an initially transient flow, which contains small-scale fluctuations corresponding to the secondary frequency (f_2D/U). Hence, the Kolmogorov scale η for the (M1, Medium)-case as given in Table II is calculated by $(\nu^3/\varepsilon)^{0.25}$, where ε denotes the local energy dissipation. The maximum ratio between the grid size Δ_c and the Kolmogorov scale, Δ_c/η, within the level-6 grid region is approximately 3.5, implying that the smallest flow structures are resolved[30]. Moreover, it should be noted that all the flow structures discussed in the present work are located within the level-6 grid region. Overall, the medium grid resolution with the computational domain 1 (M1, Medium) is applied in the present work to obtain grid- and domain-independent results.

REFERENCES

[1]Y. Rao, P. Zhang, Y. Xu, and H. Ke, "Experimental study and numerical analysis of heat transfer enhancement and turbulent flow over shallowly dimpled channel surfaces," International Journal of Heat and Mass Transfer **160**, 120195 (2020).

[2]P. Zhang, Y. Rao, and P. M. Ligrani, "Experimental study of turbulent flow heat transfer and pressure loss over surfaces with dense micro-depth dimples under viscous sublayer," International Journal of Thermal Sciences **177**, 107581 (2022).

[3]E. Sobhani, M. Ghaffari, and M. J. Maghrebi, "Numerical investigation of dimple effects on darrieus vertical axis wind turbine," Energy **133**, 231–241 (2017).

[4]V. D'Alessandro, G. Clementi, L. Giammichele, and R. Ricci, "Assessment of the dimples as passive boundary layer control technique for laminar airfoils operating at wind turbine blades root region typical reynolds numbers," Energy **170**, 102–111 (2019).

[5]H. Sedighi, P. Akbarzadeh, and A. Salavatipour, "Aerodynamic performance enhancement of horizontal axis wind turbines by dimples on blades: Numerical investigation," Energy **195**, 117056 (2020).

[6]Y. Xie, Y. Rao, Y. Cheng, and W. Tian, "Investigation into the laminar separation control of airfoils at low reynolds numbers by dimple vortex generators," Aerospace Science and Technology **129**, 107841 (2022).

[7]V. B. Ananthan, R. A. Akkermans, T. Hu, P. Q. Liu, and N. Rathje, "Trailing-edge noise reduction potential of a locally applied shallow dimpled surface," Journal of Sound and Vibration **525**, 116745 (2022).

[8]M. van Nesselrooij, L. Veldhuis, B. Van Oudheusden, and F. Schrijer, "Drag reduction by means of dimpled surfaces in turbulent boundary layers," Experiments in Fluids **57**, 1–14 (2016).

[9]P. Spalart, M. Shur, M. Strelets, A. Travin, K. Paschal, and S. Wilkinson, "Experimental and numerical study of the turbulent boundary layer over shallow dimples," International Journal of Heat and Fluid Flow **78**, 108438 (2019).

[10]F. Gattere, A. Chiarini, and M. Quadrio, "Dimples for skin-friction drag reduction: status and perspectives," Fluids **7**, 240 (2022).

[11]G. Kovalenko, V. Terekhov, and A. Khalatov, "Flow regimes in a single dimple on the channel surface," Journal of Applied Mechanics and Technical Physics **51**, 839–848 (2010).

[12]C. Tay, Y. Chew, B. Khoo, and J. Zhao, "Development of flow structures over dimples," Exper-

imental Thermal and Fluid Science **52**, 278–287 (2014).

[13]J. Lan, Y. Xie, and D. Zhang, "Effect of leading edge boundary layer thickness on dimple flow structure and separation control," Journal of Mechanical Science and Technology **25**, 3243–3251 (2011).

[14]S. Isaev, A. Leont'ev, P. Baranov, and A. Usachev, "Bifurcation of vortex turbulent flow and intensification of heat transfer in a hollow," in *Doklady Physics*, Vol. 45 (Springer, 2000) pp. 389–391.

[15]J. Turnow, N. Kornev, S. Isaev, and E. Hassel, "Vortex mechanism of heat transfer enhancement in a channel with spherical and oval dimples," Heat and Mass Transfer **47**, 301–313 (2011).

[16]M. Manhart, F. Tremblay, and R. Friedrich, "MGLET: a parallel code for efficient DNS and LES of complex geometries," in *Parallel Computational Fluid Dynamics 2000*, edited by C. Jenssen, H. Andersson, A. Ecer, N. Satofuka, T. Kvamsdal, B. Pettersen, J. Periaux, and P. Fox (North-Holland, Amsterdam, 2001) pp. 449–456.

[17]M. Manhart and R. Friedrich, "DNS of a turbulent boundary layer with separation," International Journal of Heat and Fluid Flow **23**, 572–581 (2002).

[18]N. Peller, A. L. Duc, F. Tremblay, and M. Manhart, "High-order stable interpolations for immersed boundary methods," International Journal for Numerical Methods in Fluids **52**, 1175–1193 (2006).

[19]M. Manhart, "A zonal grid algorithm for DNS of turbulent boundary layers," Computers & Fluids **33**, 435–461 (2004).

[20]A. Ashrafian, H. I. Andersson, and M. Manhart, "DNS of turbulent flow in a rod-roughened channel," International Journal of Heat and Fluid Flow **25**, 373–383 (2004).

[21]L. Unglehrt and M. Manhart, "Decomposition of the drag force in steady and oscillatory flow through a hexagonal sphere pack," Journal of Fluid Mechanics **974**, A32 (2023).

[22]F. Jiang, H. I. Andersson, J. P. Gallardo, and V. L. Okulov, "On the peculiar structure of a helical wake vortex behind an inclined prolate spheroid," Journal of Fluid Mechanics **801**, 1–12 (2016).

[23]C. Tian, J. Zhu, and L. E. Holmedal, "Coexistence of natural and forced vortex dislocations in step cylinder flow," Physics of Fluids **35** (2023).

[24]F. Jiang, B. Pettersen, and H. I. Andersson, "Turbulent wake behind a concave curved cylinder," Journal of Fluid Mechanics **878**, 663–699 (2019).

[25]Y. Zhang, K. Liu, H. Xian, and X. Du, "A review of methods for vortex identification in hydro-turbines," Renewable and Sustainable Energy Reviews **81**, 1269–1285 (2018).

[26]M. Hack and T. Zaki, "Streak instabilities in boundary layers beneath free-stream turbulence," Journal of Fluid Mechanics **741**, 280–315 (2014).

[27]W. Huang, Z. Wang, D. Xiao, G. Xi, and X. Mao, "Transition induced by wall-normal vibration in flow around a flat plate with roughness," Journal of Fluid Mechanics **940** (2022).

[28]M. Landahl, "A note on an algebraic instability of inviscid parallel shear flows," Journal of Fluid Mechanics **98**, 243–251 (1980).

[29]L. Brandt and D. S. Henningson, "Transition of streamwise streaks in zero-pressure-gradient boundary layers," Journal of Fluid Mechanics **472**, 229–261 (2002).

[30]P. Moin and K. Mahesh, "Direct numerical simulation: a tool in turbulence research," Annual Review of Fluid Mechanics **30**, 539–578 (1998).